Electronic Supplementary Information (ESI) for

Cobalt Germanide Precipitates Indirectly Improve the Properties of Thermoelectric Germanium Antimony Tellurides

by

**Daniel Souchay$^{a)}$, Stefan Schwarzmüller$^{a)}$, Hanka Becker$^{b)}$, Stefan Kante$^{b)}$,
G. Jeffrey Snyder$^{c)}$, Andreas Leineweber$^{b)}$, Oliver Oeckler$^{*,a)}$**

a) Institute for Mineralogy, Crystallography and Materials Science; Faculty of Chemistry and Mineralogy, Leipzig University, Scharnhorststr. 20, 04275 Leipzig, Germany.
b) Institute of Materials Science, TU Bergakademie Freiberg, Gustav-Zeuner-Str. 5, 09599 Freiberg, Germany.
c) Department of Materials Science and Engineering, Northwestern University Evaston, IL 60208, United States.

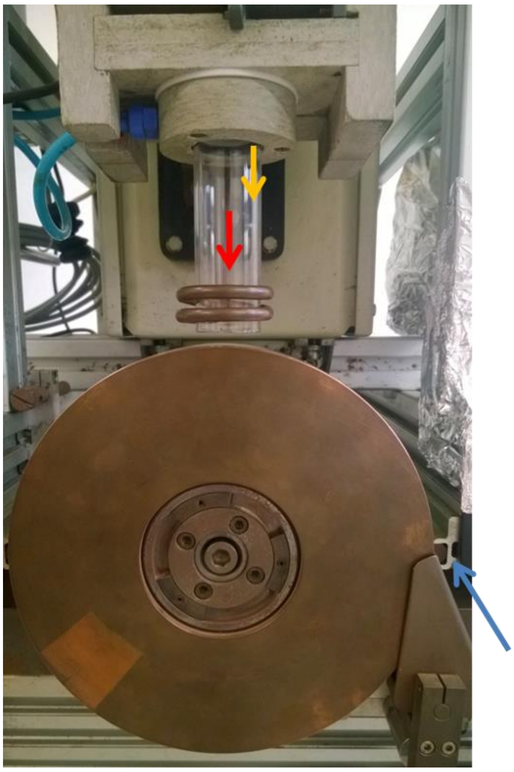

Figure S1: Synthesis of samples by melt spinning (MS): The directions of argon flow creating a protective atmosphere around the silica glass nozzle and the copper wheel are represented by the yellow arrow (0.2 bar argon) and the blue arrow (1.2 bar argon), respectively. The samples (~ 10 g) are placed in the center of the coil of the HF furnace (max. 300 kHz) and the power is increased slowly until the samples are at red heat (molten). As soon as this happens, the ejection pressure (0.35 bar argon) is applied in direction of the red arrow to cast the (re)molten sample through the nozzle onto the copper wheel of the melt spinning device, which rotates at 1500 rpm. The distance from the silica glass nozzle to the copper wheel is 0.3 mm.

Table S1: Parameters used for spark plasma sintering (SPS).

vacuum	pressure	heating program	cooling program
SPS chamber evacuated 5 min up to 6 · 10^{-1} mbar then flooded with argon up to 900 mbar	3 min up to 8 kN ≈ 70 MPa	100 K/min up to 475 °C, dwell time 15 min	furnace off, sample taken out of the chamber after 10 min

Table S2: C_p according to the Dulong-Petit relationship and densities measured using Archimedes' principle for samples used in the present study. All densities were higher than 98 % of the calculated X-ray densities of the matrix material.

nominal composition	calculated X-ray density (g cm^{-3}) of the matrix phase from Rietveld refinement (MS / SPS)	density (g cm^{-3}) of bulk sample	*Cp* (J g^{-1}K^{-1}) (Dulong-Petit)
GeTe	6.22	6.10(3)	0.249
$(GeTe)_{12}Sb_2Te_3$	6.26	6.21(3)	0.239
$(GeTe)_{17}Sb_2Te_3$	6.23	6.25(3)	0.241
$(GeTe)_{19}Sb_2Te_3$	6.24	6.17(3)	0.242
$(Co_5Ge_7)_{0.0026}GeTe$	6.22	6.19(3)	0.250
$(CoGe_2)_{0.01}GeTe$	6.21	6.20(3)	0.250
$(CoGe_2)_{0.15}(GeTe)_{12}Sb_2Te_3$	6.26	6.19(3)	0.240
$(CoGe_2)_{0.2}(GeTe)_{17}Sb_2Te_3$	6.24	6.19(3)	0.243
$(CoGe_2)_{0.22}(GeTe)_{19}Sb_2Te_3$	6.22	6.21(3)	0.243
nominal composition	calculated X-ray density (g cm^{-3}) of the matrix phase from Rietveld refinement (water quenched)	density (g cm^{-3}) of bulk sample	*Cp* (J g^{-1}K^{-1}) (Dulong-Petit)
GeTe	6.22	6.22(3)	0.249
$(Co_5Ge_7)_{0.0026}GeTe$	6.23	6.30(3)	0.250
$(CoGe_2)_{0.01}GeTe$	6.23	6.30(3)	0.250

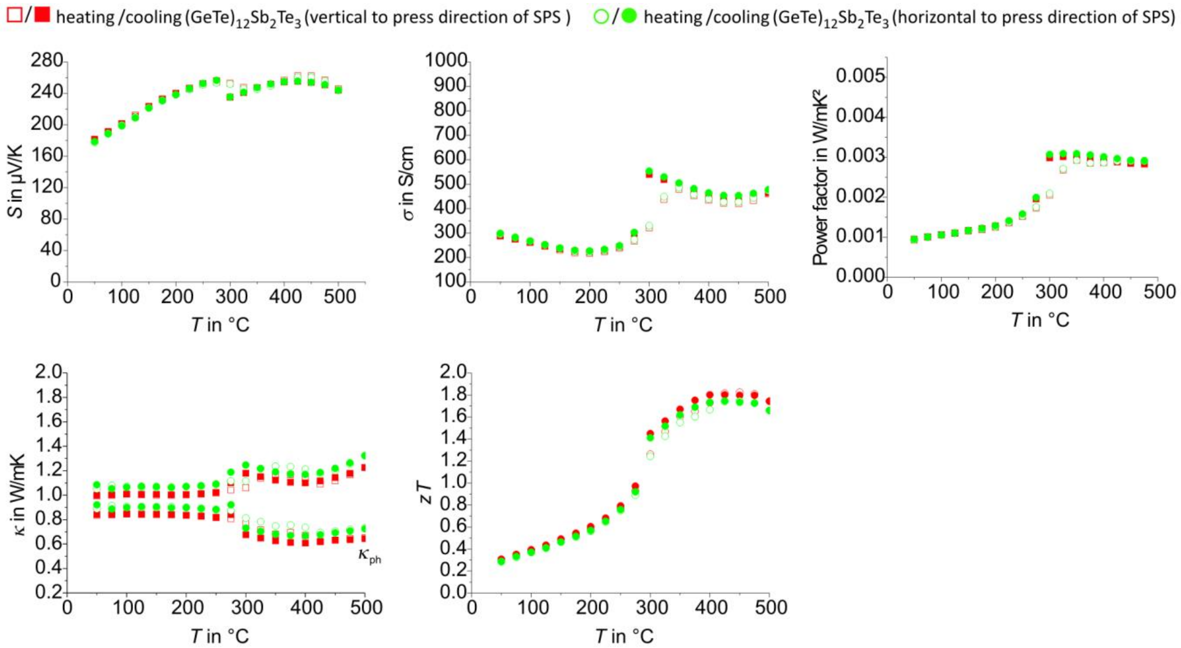

Figure S2: Thermoelectric properties of pristine $(GeTe)_{12}Sb_2Te_3$ prepared by MS / SPS (all data points of the were merged from 3 cycles from 50 °C to-500 °C, discarding the first heating curve): Seebeck coefficient S top left, electrical conductivity σ top middle, power factor top right, thermal conductivity κ and corresponding phononic part κ_{ph} (calculated according to the Wiedemann-Franz relationship with a Lorenz number L derived from S according to $L = 1.5 + e^{(-|S|/116)}$ where L is in 10^{-8} W Ω K^{-2} and S in μV K^{-1}) bottom left, zT value middle bottom; samples cut from pellets in different directions (cf. legend).

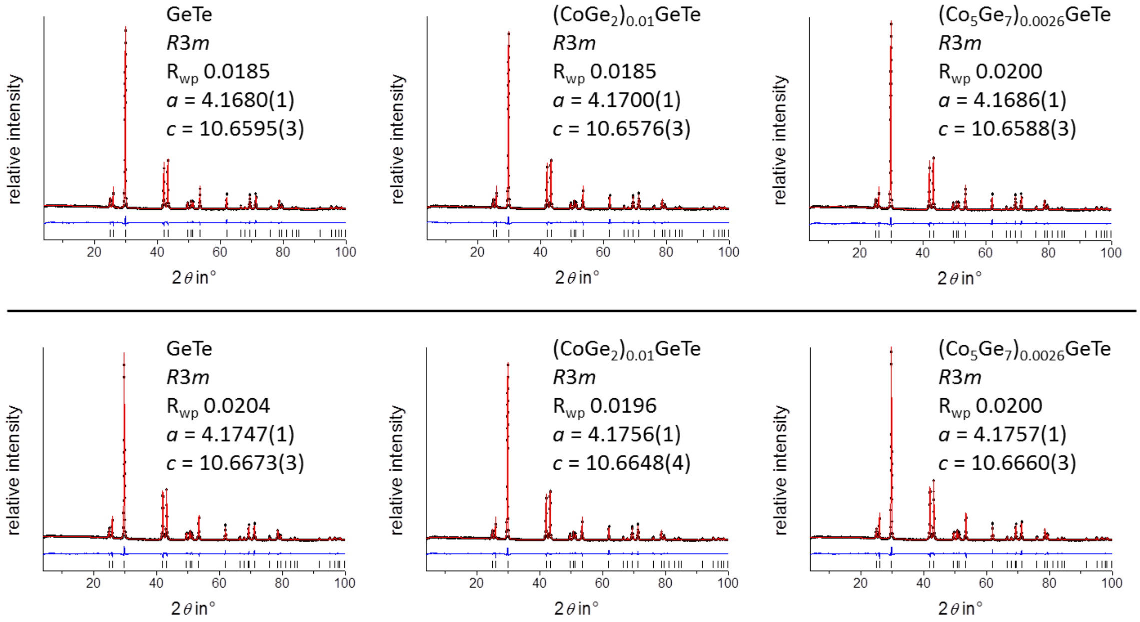

Figure S3: Top: PXRD patterns of samples with the compositions GeTe (left), (CoGe$_2$)$_{0.01}$GeTe (middle) and (Co$_5$Ge$_7$)$_{0.0026}$GeTe (right) after melt spinning (MS) and spark plasma sintering (SPS); bottom: corresponding PXRD patterns recorded after thermoelectric measurements; Rietveld refinements taking into account atomic parameters of GeTe-type structure (*R*3*m*) for the GeTe matrix (from reference 1, Stephens' model [2] was used to model anisotropic peak broadening); experimental (black points) and calculated (red) patterns, difference plot (blue) and reflection positions (black lines, bottom). Note that cobalt germanides were not included in the refinement due to their very small overall fraction.

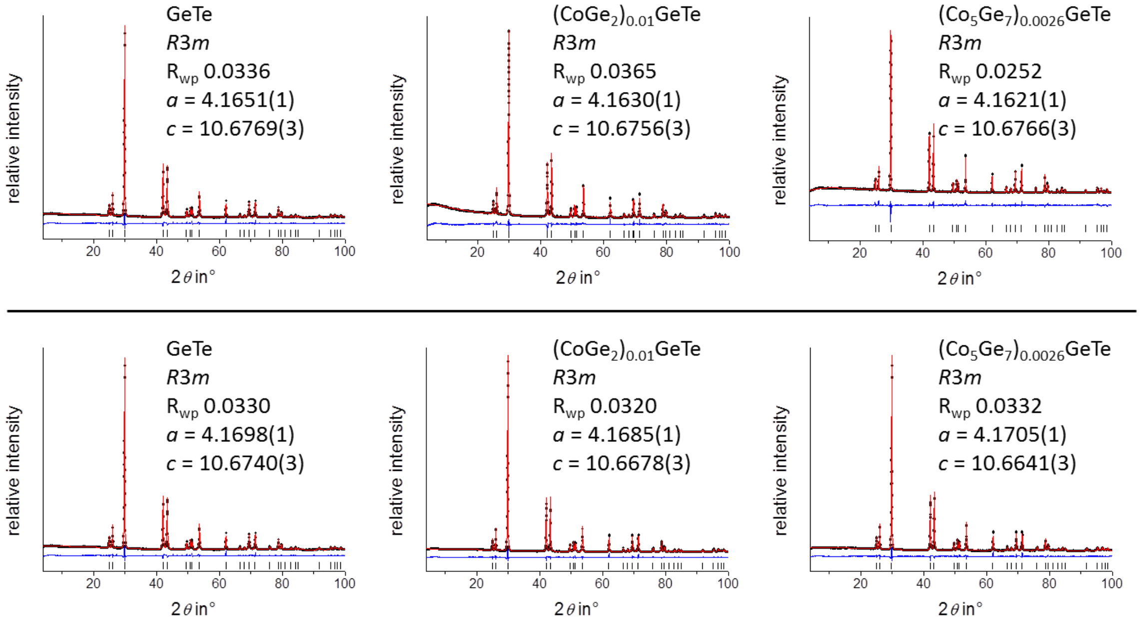

Figure S4: Top: PXRD patterns of samples with the compositions GeTe (left), (CoGe$_2$)$_{0.01}$GeTe (middle) and (Co$_5$Ge$_7$)$_{0.0026}$GeTe (right) after quenching in water and annealing (1d at 590 °C); bottom: corresponding PXRD patterns recorded after thermoelectric measurements; Rietveld refinements taking into account atomic parameter of GeTe-type structure (*R*3*m*) for the GeTe matrix (from reference 1, Stephens' model [2] was used to model anisotropic peak broadening); experimental (black points) and calculated (red) patterns, difference plot (blue) and reflection positions (black lines, bottom). Note that cobalt germanides were not included in the refinement due to their very small overall fraction.

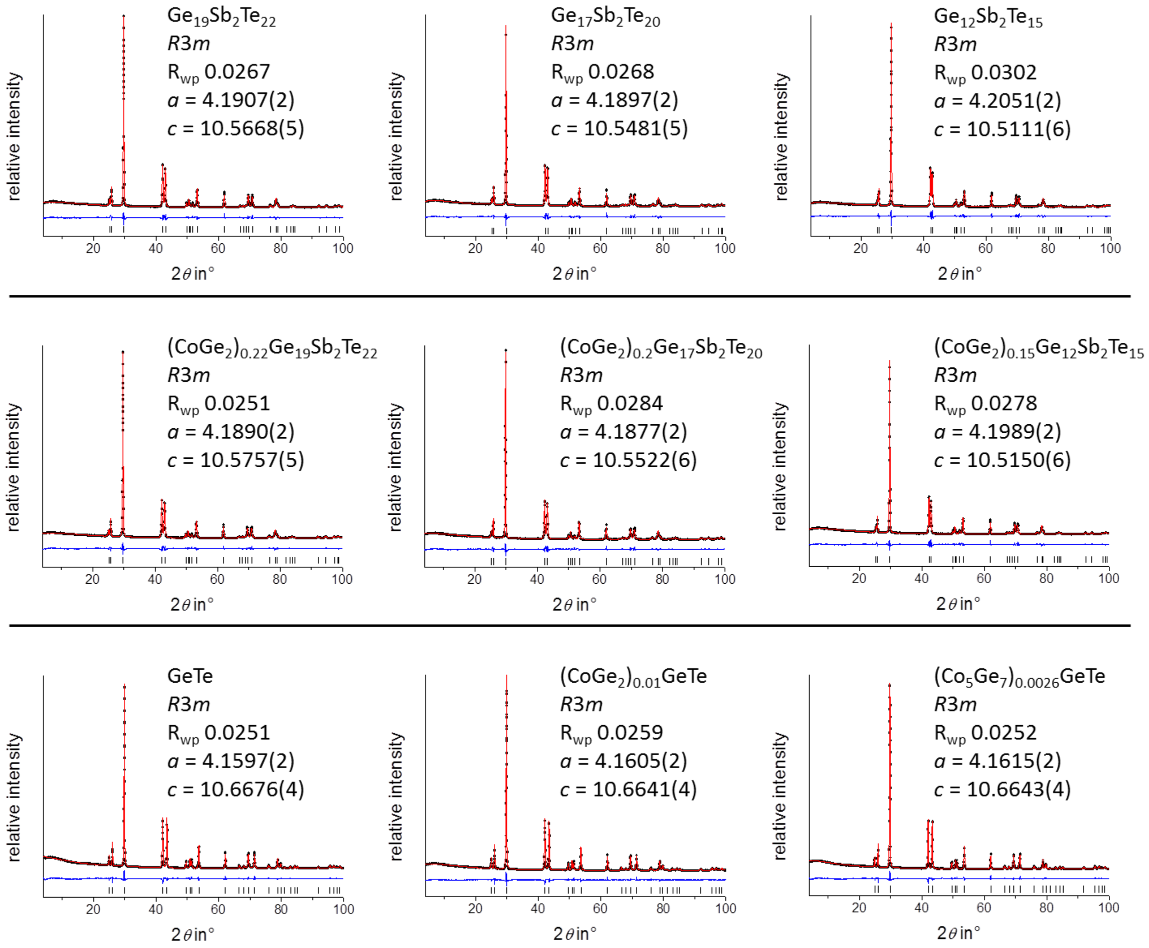

Figure S5: Top: PXRD patterns of samples with the compositions given in the diagrams, after melt spinning (but without SPS); Rietveld refinements taking into account atomic parameters of GeTe-type structure (*R*3*m*) for the GeTe matrix (from reference 1; for GST matrices, mixed occupation of Ge and Sb on the Wyckoff site 4*b* was taken into account; Stephens' model[2] was used to model anisotropic peak broadening); experimental (black points) and calculated (red) data, difference plot (blue) and reflection positions (black lines, bottom). Note that cobalt germanides were not included in the refinement due to their very small overall fraction.

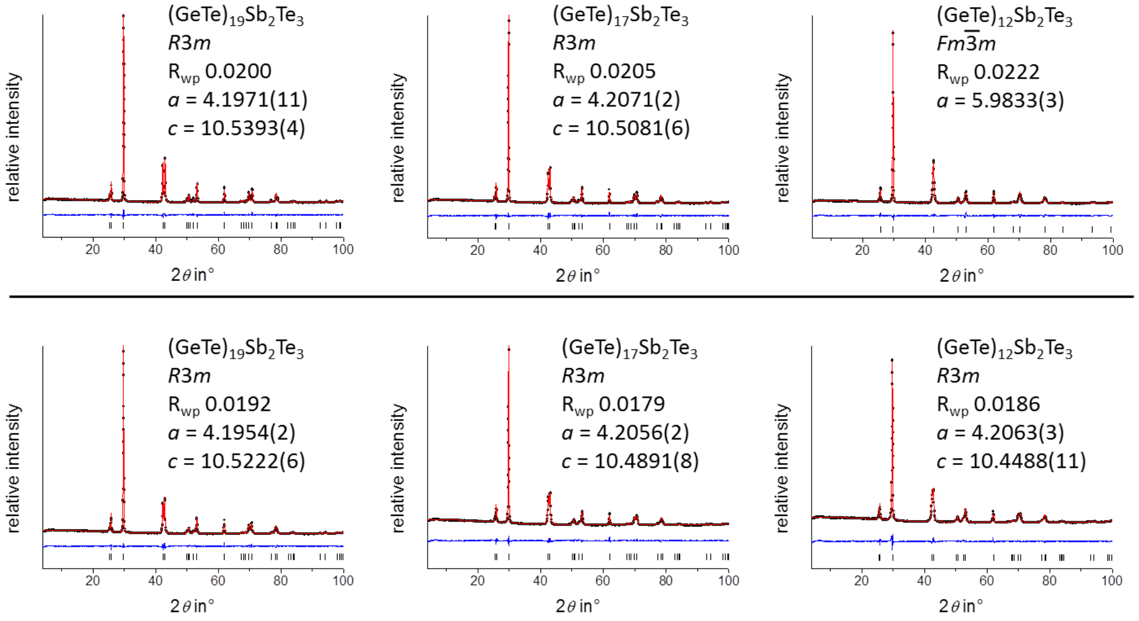

Figure S6: top: PXRD patterns of samples with the compositions given in the diagrams, after melt spinning (MS) and spark plasma sintering (SPS); bottom: PXRD patterns of the corresponding samples after thermoelectric measurements; Rietveld refinements taking into account atomic parameters of GeTe-type structure ($R3m$) for the GeTe matrix (from reference 1; for GST matrices, the mixed occupation of Ge and Sb on the Wyckoff site 4*b* was taken into account); exception for $(GeTe)_{12}Sb_2Te_3$ after MS / SPS: the atomic parameters of NaCl-type structure ($Fm\bar{3}m$) from reference 3 were used; Stephens' model [2] was used to model anisotropic peak broadening; experimental (black points) and calculated (red) data, difference plot (blue) and reflection positions (black lines, bottom).

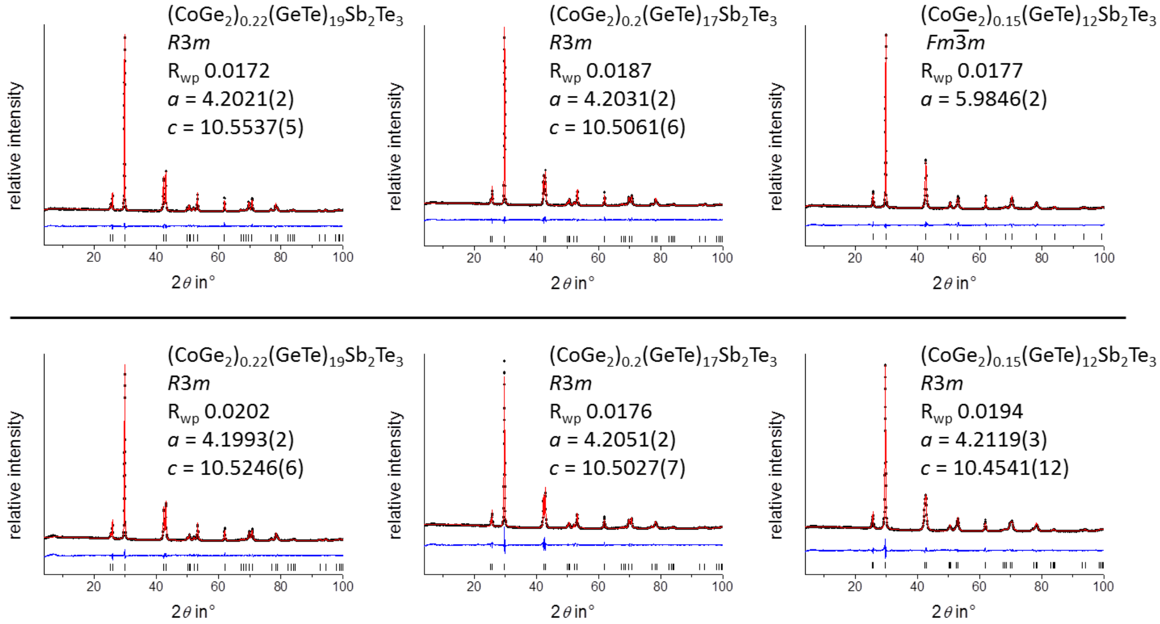

Figure S7: top: PXRD patterns of samples with the compositions given in the diagrams, after melt spinning (MS) and spark plasma sintering (SPS); bottom: PXRD patterns of the corresponding samples after thermoelectric measurements; Rietveld refinements taking into account atomic parameters of GeTe-type structure ($R3m$) of the matrix (from reference 1; for GST matrices, mixed occupation of Ge and Sb on Wyckoff site 4*b* was taken into account); exception for $(GeTe)_{12}Sb_2Te_3$ matrix after MS / SPS: atomic parameters of NaCl-type structure ($Fm\bar{3}m$) from ref. 3 were used; Stephens' model [2] was used to model anisotropic peak broadening; experimental (black points) and calculated (red) patterns, difference plot (blue) and reflection positions (black lines, bottom). Note that cobalt germanides were not included in the refinement due to their very small overall fraction.

Table S3: Results of SEM-EDX measurements for the matrix phase (MS/SPS) (left to the right) of samples with the nominal compositions listed in the table; data averaged from 9 single measurement points for each sample; all measurements performed after thermoelectric measurements.

sample composition	$(CoGe_2)_{0.15}(GeTe)_{12}Sb_2Te_3$,	$(CoGe_2)_{0.2}(GeTe)_{17}Sb_2Te_3$	$(CoGe_2)_{0.22}(GeTe)_{19}Sb_2Te_3$	$(CoGe_2)_{0.01}GeTe$	$(Co_5Ge_7)_{0.0026}GeTe$
formula	$(GeTe)_{12}Sb_2Te_3$ (matrix)	$(GeTe)_{17}Sb_2Te_3$ (matrix)	$(GeTe)_{19}Sb_2Te_3$ (matrix)	GeTe (matrix)	GeTe (matrix)
at.-% meas.	**Ge**: 40.6(7) **Sb**: 7.0(5) **Te**: 52.4(7)	**Ge**: 43.4(6) **Sb**: 5.0(4) **Te**: 51.6(5)	**Ge**: 43.1(7) **Sb**: 4.5(3) **Te**: 52.4(8)	**Ge**: 49.1(1) **Te**: 50.9(1)	**Ge**: 48.8(3) **Te**: 51.2(1)
at.-% calc.	**Ge**: 41.4 **Sb**: 6.9 **Te**: 51.7	**Ge**: 43.6 **Sb**: 5.1 **Te**: 51.3	**Ge**: 44.2 **Sb**: 4.65 **Te**: 51.16	**Ge**: 50 **Te**: 50	**Ge**: 50 **Te**: 50

Table S4: Results of SEM-EDX measurements for pristine GeTe and GST materials (MS/SPS) with the compositions $(GeTe)_{12}Sb_2Te_3$, $(GeTe)_{17}Sb_2Te_3$ and $(GeTe)_{19}Sb_2Te_3$ and GeTe, data averaged from 9 single measurements points for each sample; all measurements performed after thermoelectric measurements.

formula	$(GeTe)_{12}Sb_2Te_3$	$(GeTe)_{17}Sb_2Te_3$	$(GeTe)_{19}Sb_2Te_3$	GeTe
at.-% meas.	**Ge**: 40.4(8) **Sb**:7.0(4) **Te**: 52.6(7)	**Ge**: 42.4(6) **Sb**:5.3(5) **Te**: 52.3(7)	**Ge**: 43.0(8) **Sb**: 4.5(8) **Te**: 52.6(7)	**Ge**: 49.1(3) **Te**: 50.9(3)
at.-% calc.	**Ge**: 41.4 **Sb**: 6.9 **Te**: 51.7	**Ge**: 43.6 **Sb**: 5.1 **Te**: 51.3	**Ge**: 44.2 **Sb**: 4.65 **Te**: 51.16	**Ge**: 50 **Te**: 50

Table S5: Results of SEM-EDX measurements for the matrix phase (water quenched) of samples with the compositions GeTe (left), $(CoGe_2)_{0.01}GeTe$ (middle) and $(Co_5Ge_7)_{0.0026}GeTe$ (right); data averaged from 9 single measurement points for each sample); all measurements performed after thermoelectric measurements.

formula	GeTe (matrix)	GeTe (matrix)	GeTe (matrix)
at.-% meas.	**Ge**: 48.5(3) **Te**: 51.5(3)	**Ge**: 47.8(4) **Te**: 52.2(4)	**Ge**: 48.9(1) **Te**: 51.1(1)
at.-% calc.	**Ge**: 50 **Te**: 50	**Ge: 50 Te: 50**	**Ge**: 50 **Te**: 50

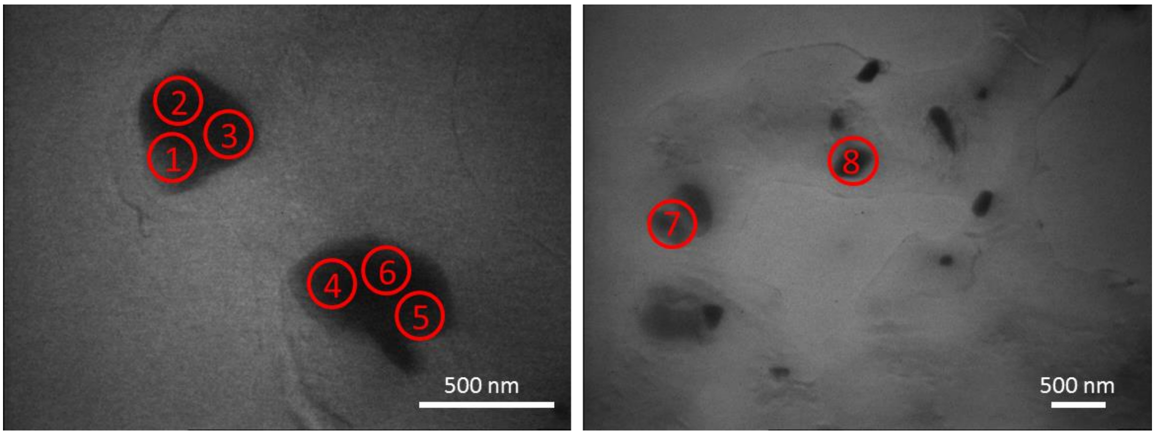

Figure S8: TEM-BF images of a (MS / SPS) sample with the nominal composition $(CoGe_2)_{0.2}Ge_{17}Sb_2Te_{20}$ after thermoelectric measurement: black spots represent the precipitates surrounded by GST matrix; red circles and numbers represent the EDX point measurements, results given in Table S6.

Table S6: TEM-EDX point measurements of precipitates (see Figure S8) in a MS/SPS sample with the composition $(CoGe_2)_{0.2}Ge_{17}Sb_2Te_{20}$.

elements	**atom% measured (points 1,4-6)**	**atom% measured; (points 2-3)**	**points 7 and 8**	**atom% calculated for Co_5Ge_7**	**atom% calculated for $Co_{0.875}Ge_2$**
Co	39.6(3)	30.5(11)	32.1(1)	41.7	30.4
Sb	0.3(1)	0.3(1)	0.2(1)		
Ge	58.1(5)	66.3(4)	66.3(4)	58.3	69.6
Te	2.1(4)	3(2)	1.5(4)		

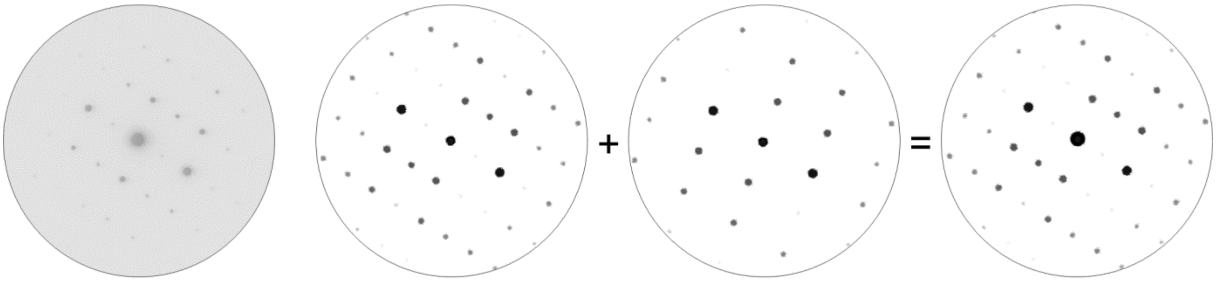

[152] simulated

[1$\bar{2}$5] simulated

twin [152] and [1$\bar{2}$5]

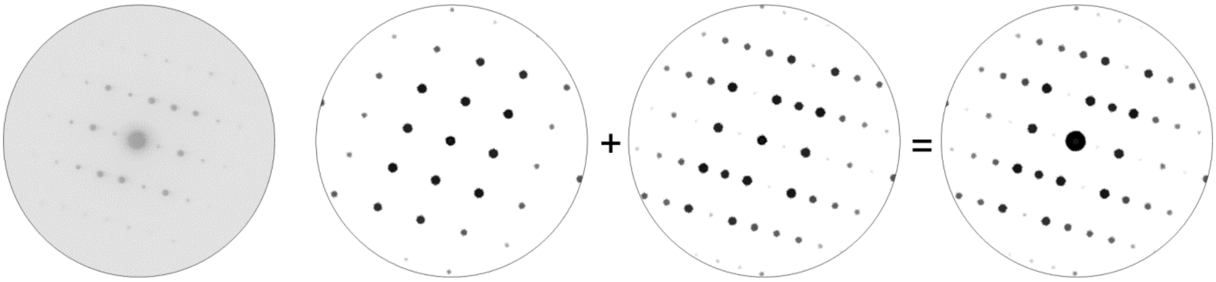

[141] simulated

[1$\bar{1}$4] simulated

twin [141] and [1$\bar{1}$4]

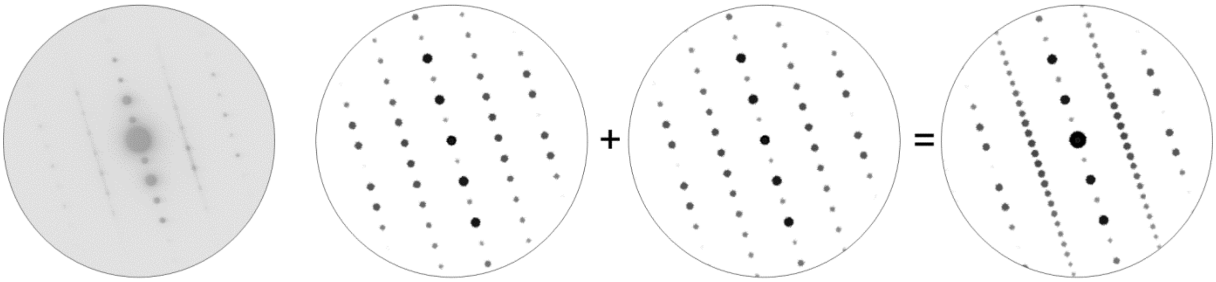

[021] simulated

[0$\bar{1}$2] simulated

twin [021] and [0$\bar{1}$2]

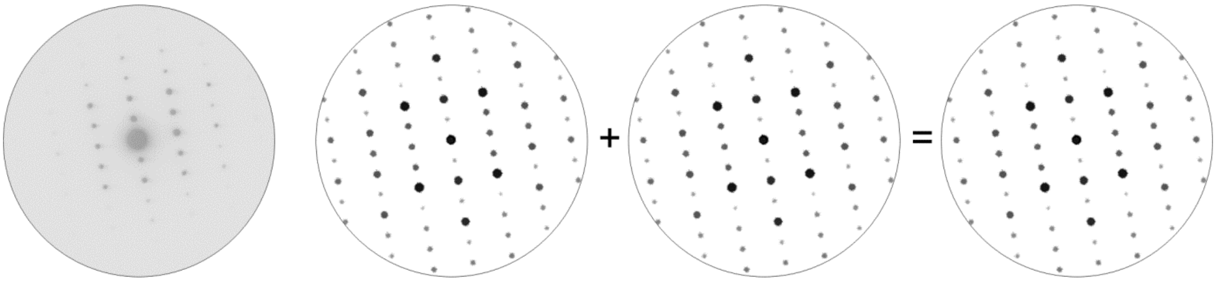

[010] simulated

[001] simulated

twin [010] and [001]

Figure S9: SAED patterns of a twinned precipitate (twin law [1 0 0, 0 0 -1, 0 1 0]) in a sample with the nominal composition $(CoGe_2)_{0.2}(GeTe)_{17}Sb_2Te_3$ and corresponding simulated diffraction patterns of $CoGe_2$ (kinematical approximation, *Cmce* with *a* = 10.82 Å, *b* = 5.68 Å and *c* = 5.68 Å, model from ref. 4); the corresponding tilt angles are given in Fig. S10.

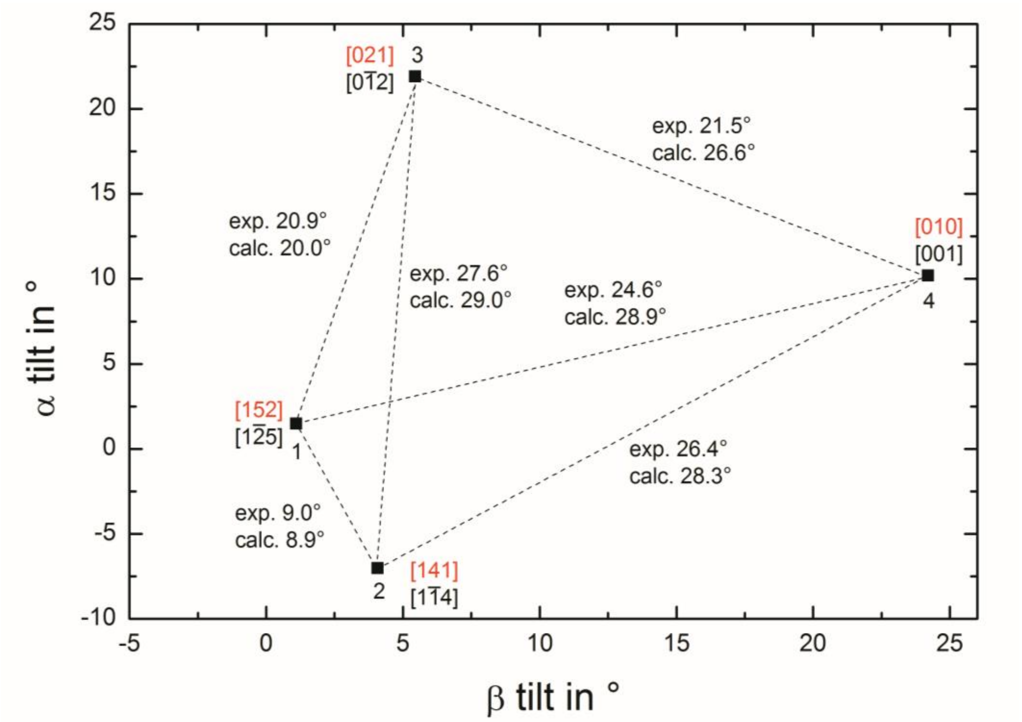

Figure S10: Experimental (exp.) and calculated (calc., based on SAED indexing) tilt angles between measured SAED patterns (see Fig. S9) with zone axes of the precipitates in (CoGe$_2$)$_{0.2}$(GeTe)$_{17}$Sb$_2$Te$_3$; calculated tilt angles are the same for red and black indices due to twinning according to twin law [1 0 0, 0 0 -1, 0 1 0].

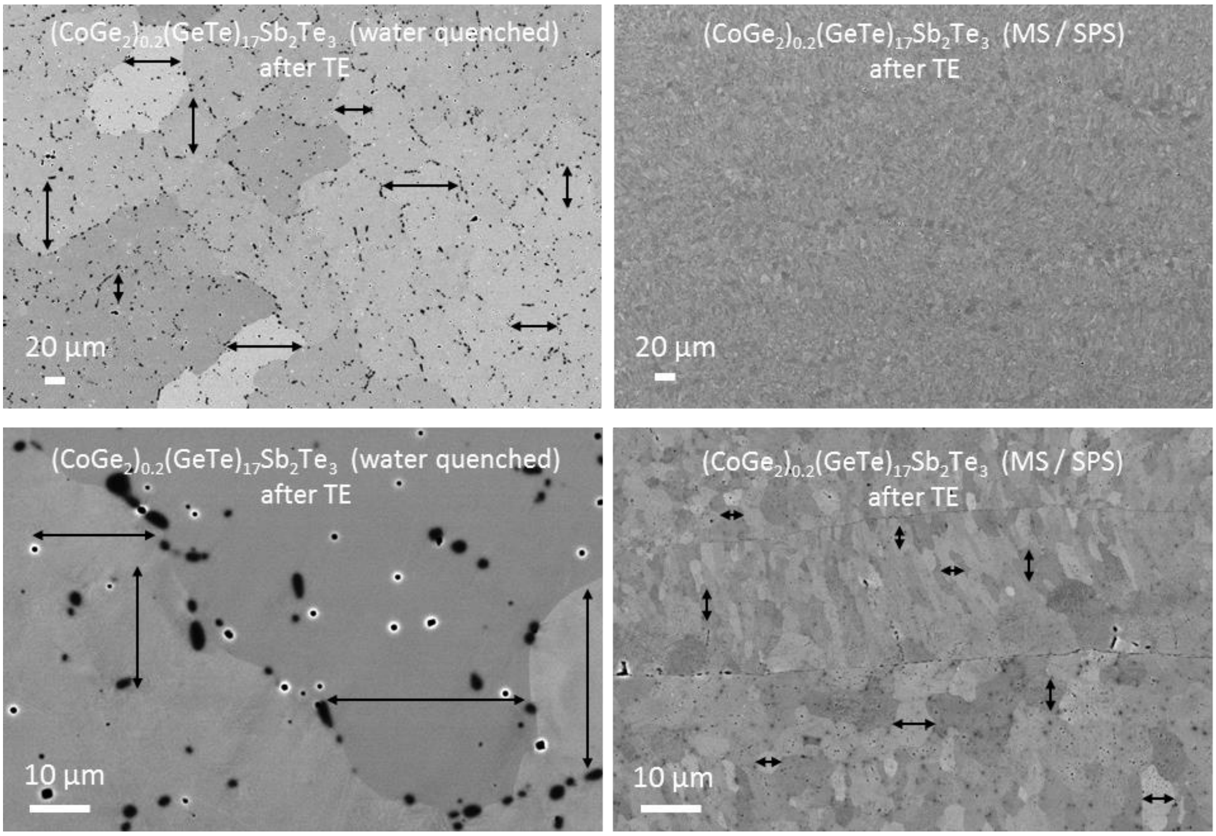

Figure S11: SEM-BSE images of polycrystalline bulk samples with the nominal composition (CoGe$_2$)$_{0.2}$(GeTe)$_{17}$Sb$_2$Te$_3$: water-quenched (left) and MS / SPS (right) with two different magnifications each: microstructure of samples after thermoelectric measurements; channeling contrast reveals individual grains (different gray levels represent backscattered intensity: light gray corresponds to high backscattering intensity); black arrows are a guide to the eyes to visualize grain and/or sub-grain sizes.

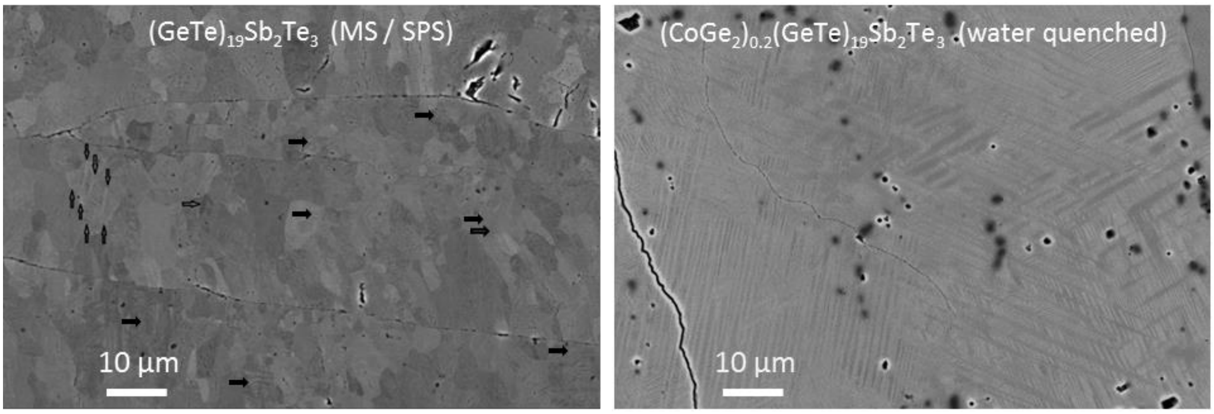

Figure S12: SEM-BSE images of polycrystalline bulk $(GeTe)_{19}Sb_2Te_3$ (left, MS / SPS) and a sample with the nominal composition $(CoGe_2)_{0.22}(GeTe)_{19}Sb_2Te_3$ (right, water quenched): microstructures after thermoelectric measurements; channeling contrast was observed between the different grains and twin domains; different gray levels represent backscattered intensity (lighter gray indicates higher backscattered intensity); both samples exhibit a twin domain structure within the (sub-)grains independent of the (sub-)grain size; black arrows are a guide to the eyes to visualize areas were these herringbone-like structure are visible in the left image.

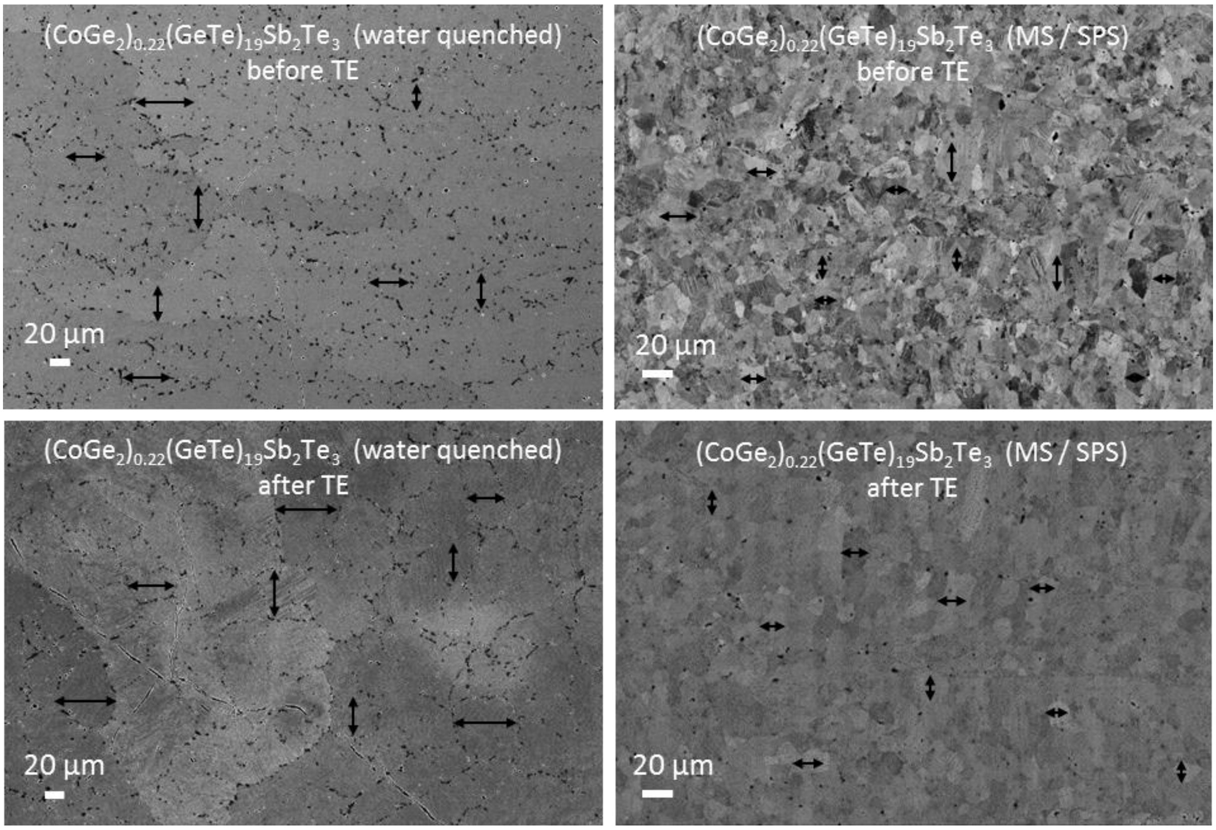

Figure S13: SEM BSE image of polycrystalline bulk samples with the composition $(CoGe_2)_{0.22}(GeTe)_{19}Sb_2Te_3$: water quenched (left) and MS / SPS (right); microstructures before and after thermoelectric measurements visualized by channeling contrast (lighter gray corresponds to higher backscattered); black arrows are a guide to the eyes to visualize that the grain and sub-grain sizes do not change significantly during thermoelectric measurements.

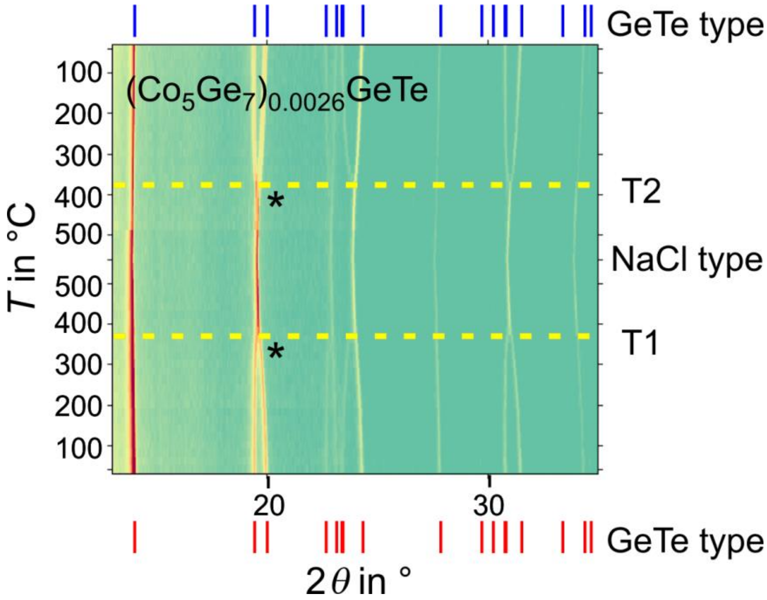

Figure S14: Temperature dependent PXRD patterns of heterostructured samples with cobalt germanides in a GeTe matrix obtained by MS / SPS: at RT, the average structure of GeTe corresponds to a variant of the rhombohedral α-GeTe type; a phase transition to a disordered NaCl-type structure takes place upon heating, and the α-GeTe-type structure is formed again upon cooling; dashed yellow lines highlight these phase transitions, which are indicated e.g. by splitting of reflections (e.g. the one marked with asterisks); red and blue reflection markers indicate the structures before heating and after cooling, respectively. Note that cobalt germanides are not visible due to their low overall fraction.

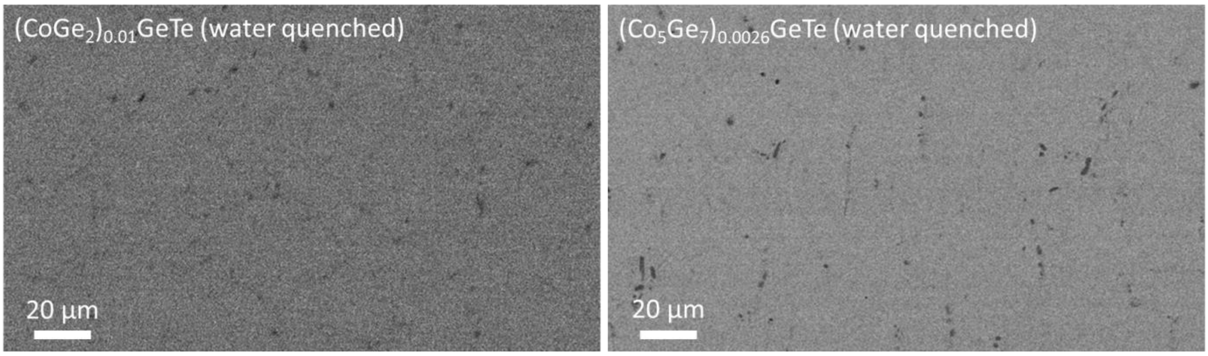

Figure S15: SEM-BSE images of heterostructured GeTe with cobalt germanide precipitates: dark spots represent cobalt germanide and germanium precipitates surrounded by GeTe matrix.

Table S7: Phase transitions of the GST matrix as evidenced by temperature-dependent PXRD measurements of $(CoGe_2)_{0.01}GeTe$, $(CoGe_2)_{0.22}(GeTe)_{19}Sb_2Te_3$, $(CoGe_2)_{0.2}Ge_{17}Sb_2Te_{20}$ and $(CoGe_2)_{0.15}(GeTe)_{12}Sb_2Te_3$); hystereses are caused by vacancy diffusion or and partial ordering during heating and cooling as reported in references 5-8. Note that the hystereses visible in the thermoelectric measurements of GST samples (e.g. in σ, Fig. 4, S16 and S17) do not exactly correspond to the phase transition temperatures, which can be attributed to a temperature gradient in the samples during measurements of Seebeck coefficient and electrical conductivity.

nominal composition	Phase transition according to PXRD (heating)	phase transition temperature (heating)	phase transition according to PXRD (cooling)	phase transition temperature (cooling)
$(CoGe_2)_{0.01}GeTe$	GeTe-type → NaCl-type	~380	NaCl-type → GeTe type	~380 °C
$(CoGe_2)_{0.22}(GeTe)_{19}Sb_2Te_3$	GeTe-type → NaCl-type	~380	NaCl-type → GeTe type	~280 °C
$(CoGe_2)_{0.2}(GeTe)_{17}Sb_2Te_3$	GeTe-type →NaCl-type	~310	NaCl-type → GeTe type	~280 °C
$(CoGe_2)_{0.15}(GeTe)_{12}Sb_2Te_3$	metastable phase (pseudo cubic) →NaCl-type	~320	NaCl-type → GeTe type	~280 °C

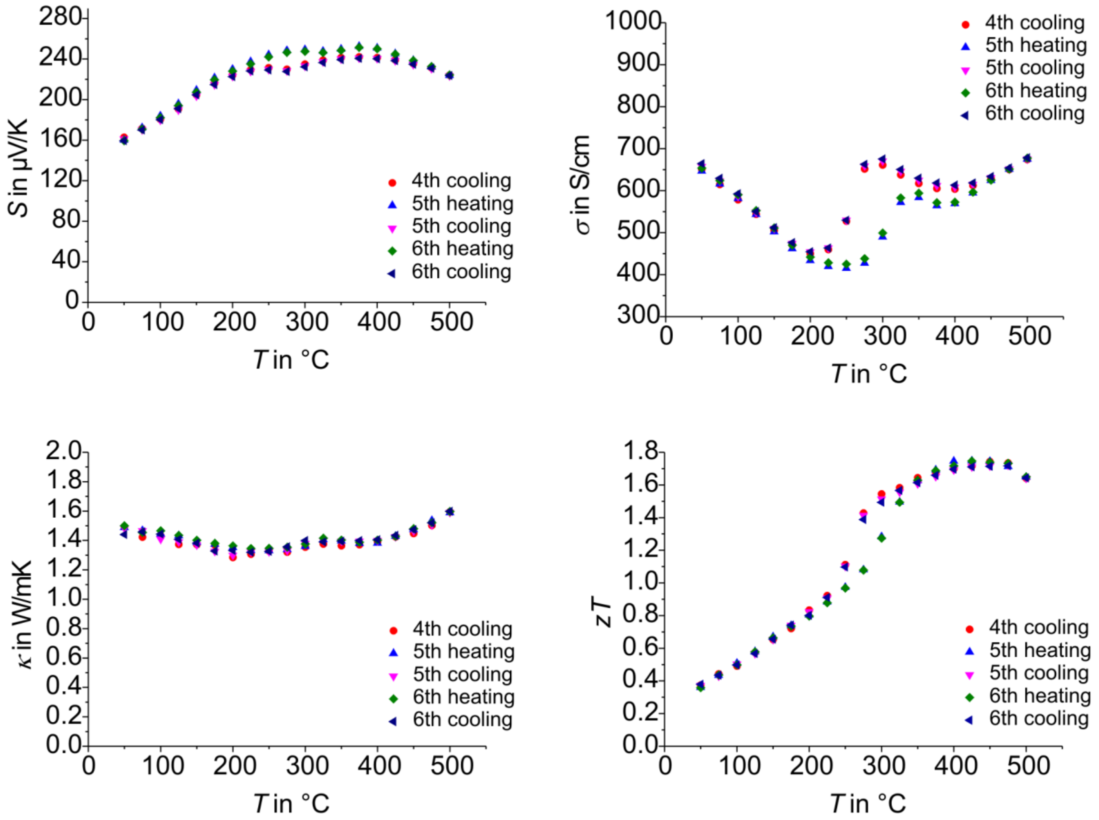

Figure S16: Thermoelectric properties of a sample with the nominal composition $(CoGe_2)_{0.22}(GeTe)_{19}Sb_2Te_3$ (MS / SPS): three consecutive measurement cycles from 50 - 500 °C (after three previous cycles up to 300 °C): Seebeck coefficient top left, electrical conductivity top right, thermal conductivity bottom left, *zT* value bottom right.

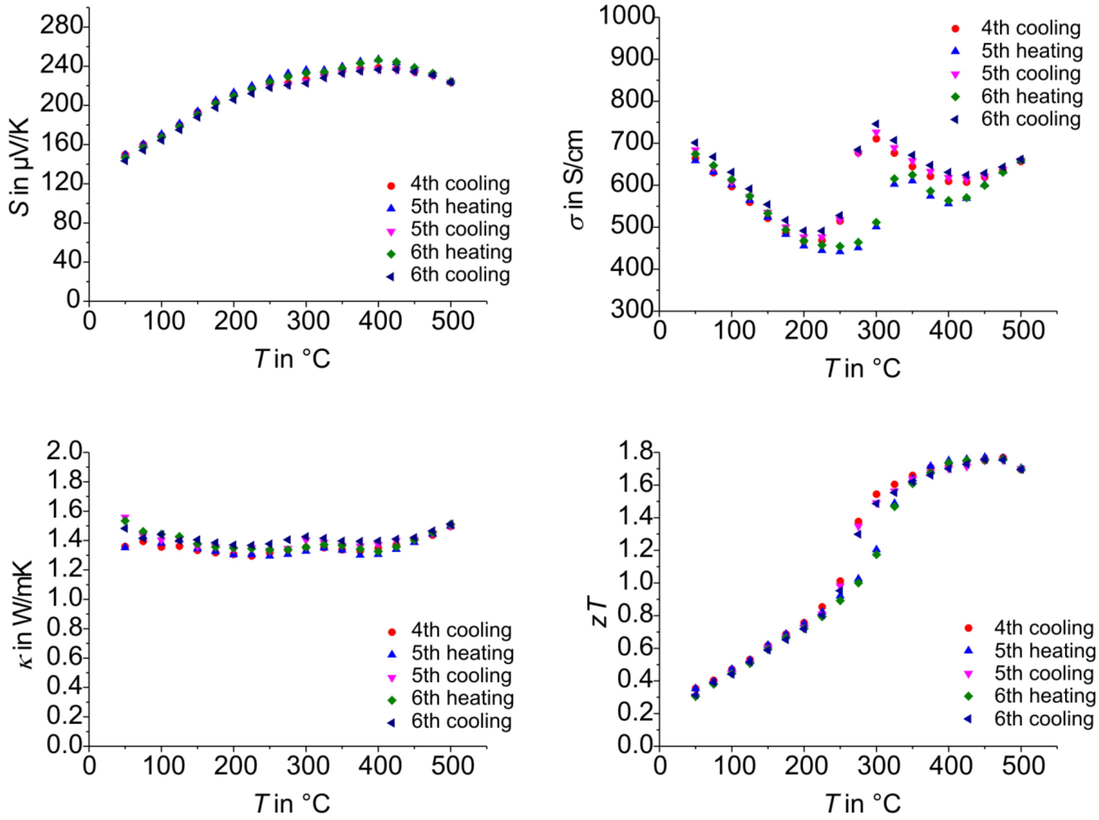

Figure S17: Thermoelectric properties of $(GeTe)_{19}Sb_2Te_3$ (MS / SPS) for three consecutive measurement cycles from 50 °C to 500 °C (after three previous cycles up to 300 °C): Seebeck coefficient top left, electrical conductivity top right, thermal conductivity bottom left, *zT* value bottom right.

Modelling of transport properties and thermoelectric data [9,10]

The effective charge charrier mass m^* is determined by the measured Hall carrier density $n_{\mathrm{H}} = n_{\mathrm{c}}/r_{\mathrm{H}}$ (assuming a spherical Fermi surface, n_{c} = chemical charrier concentration r_{H} = calculated Hall factor) by using two equations:

$$n_{\mathrm{c}} = 4\pi \left(\frac{2m^* k_{\mathrm{B}} T}{h^2}\right)^{\frac{3}{2}} F_{1/2}(\eta)$$

and

$$r_{\mathrm{H}} = \frac{3F_{1/2}(\eta) F_{-1/2}(\eta)}{4F_0(\eta)^2}$$

Further, the electron chemical potential η is estimated from the measured Seebeck coefficient S at a given temperature by numerical methods:

$$S(\eta) = \frac{k_B}{e}\left(2\frac{F_1(\eta)}{F_0(\eta)} - \eta\right)$$

with the Fermi integrals $F(\eta)$ being defined as:

$$F_x(\eta) = \int f e^x \mathrm{d}\varepsilon = \int \frac{\varepsilon^x \mathrm{d}\varepsilon}{1 + \exp(\varepsilon - \eta)}$$

Under the assumption of SPB behavior, the maximum zT is calculated taking the Hall carrier concentration into account by using:

$$zT = \frac{S^2}{L + (\psi\beta)^{-1}}$$

with β parameter,

$$\beta = \mu_0 \left(\frac{m^*}{m_{\mathrm{e}}}\right)^{3/2} \frac{T^{5/2}}{\kappa_{\mathrm{ph}}}$$

the mobility parameter μ_0,

$$\mu_0 = \frac{\mu_{\mathrm{H}} F_{-1/2}(\eta)}{2F_0(\eta)}$$

the ψ function,

$$\psi = \frac{8}{3}\pi e \left(\frac{2m_{\mathrm{e}} k_{\mathrm{B}}}{h^2}\right)^{\frac{3}{2}} F_0(\eta)$$

the Lorenz number $L(\eta)$,

$$L(\eta) = \frac{{k_{\mathrm{B}}}^2}{e^2}\left(\frac{3F_0(\eta)F_2(\eta) - 4F_1(\eta)^2}{F_0(\eta)^2}\right)$$

and the phononic part κ_{ph}, which was calculated from the measured electrical conductivity σ and the thermal conductivity κ:

$$\kappa_{\mathrm{ph}} = \kappa - L(\eta)\sigma T$$

References

1 P. B. Pereira, I. Sergueev, S. Gorsse, J. Dadda, E. Müller and R. P. Hermann, *Phys. Status Solidi B*, 2013, **7**, 1300–1307.
2 P. W. Stephens, *J. Appl. Crystallogr.* 1999, **32**, 281–289.
3 T. Matsunaga, R. Kojima, N. Yamada, K. Kifune, Y. Kubota, Y. Tabata and M. Takata, *Inorg. Chem.*, 2006, **45**, 2235–2241.
4 K. Cenzual, L. M. Gelato, M. Penzo and E. Parthé, *Acta Crystallogr. Sect. B,* 1991, **47**, 433–439.
5 T. Rosenthal, P. Urban, K. Nimmrich, L. Schenk, J. de Boor, C. Stiewe and O. Oeckler, *Chem. Mater.*, 2014, **26**, 2567–2578.
6 P. Urban, M. N. Schneider and O. Oeckler, *J. Solid State Chem.*, 2015, **227**, 223–231.
7 M. N. Schneider, X. Biquard, C. Stiewe, T. Schröder, P. Urban and O. Oeckler, *Chem. Commun.*, 2012, **48**, 2192–2194.
8 P. Urban, M. N. Schneider, M. Seemann, J. P. Wright and O. Oeckler, *Z. Kristallogr.*, 2015, **230**, 369–384.
9 A. F. May and G. J. Snyder in: *Thermoelectric and its Energy Harvesting* (ed.: D. M. Rowe), CRC Press, Boca Raton, 2012, ch. 11, pp. 1-18.
10 S. D. Kang and G. J. Snyder, arXiv:1710.06896v2, 1-5.